Dose Reduction in Medical Radiography: Advancing Veterinary Diagnostic Solutions

Huseyin Yavuz Kocaova[1], Nina Tunçel, Nuri Unal[1]

1 Akdeniz University

Funding: The authors gratefully acknowledge the partial financial support by -Ministry of Industry and Technology B.14.2.KSG.4.07.00.00-150-1392 - Akdeniz University Rectorate Scientific Research Center, (AU-BAP-FYL1787).

Potential competing interests: No potential competing interests to declare.

Abstract

In this study, we investigated photon attenuation using an anti-scatter lead grid with a flat panel detector (FPD) and aimed to mitigate it by implementing a linear array detector (LAD). We developed a mechanical system that facilitates X-ray scans using the LAD. For comparison, we selected a standard FPD unit. To assess the differences in entrance skin dose (ESD) between the LAD and FPD systems, we initially utilized anthropomorphic phantoms, followed by water phantoms for exposure tests. Results showed that at a water depth of 10 cm, the ESD from the LAD was 22% lower than that from the FPD. At 30 cm this ratio was increased up to 40%. As water thickness increased, the benefits of using LAD became more evident, demonstrated by a lower ESD. This finding highlights the potential utility of implementing this equipment in veterinary radiography, particularly for imaging animals and their anatomical sites with thicker tissues.

Hüseyin Yavuz Kocaova[1,a], **Nina Tunçel**[1,b], and **Nuri Ünal**[1,c]

[1] *Department of Physics, Akdeniz University, Antalya, Turkey*

[a] ORCID iD: 0000-0002-6484-3985

[b] ORCID iD: 0000-0002-3306-1577

[c] ORCID iD: 0000-0002-4196-5568

Keywords: Anti-scatter Pb grid, entrance skin dose, flat panel detector, linear array detector, veterinary radiographic imaging.

1. Introduction

X-ray imaging is crucial for diagnosing medical conditions, but it comes with the risk of ionizing radiation exposure. While

advancements in technology aim to reduce this risk, it is important for both healthcare providers and patients to be aware of and minimize unnecessary exposure to radiation during diagnostic procedures. During X-ray diagnostic patients also receive ionizing radiation. Nowadays a significant part of the total dose in our daily lives is due to the increase in X-ray imaging [1][2][3]. In developed countries, individuals typically receive an average radiation dose of 0.2 to 2.2 millisieverts (mSv) per year from X-rays [4]. In routine diagnostic imaging examinations such as mammography, the dose becomes even more important [5]. In veterinary radiography, scintigraphy and ultrasonography are frequently utilized for diagnosing conditions equine and cattle, particularly when conventional X-ray equipment faces challenges or limitations, such as regulatory constraints or difficulties in imaging beyond the extremities of these large animals [6][7][8].

In physics, attenuation refers to the reduction in the intensity of a signal or beam as it passes through a medium and explained by Beer-Lambert Law as $I_1=I_0\, e^{-(\mu.x)}$ where I_0 is incident, I_1 is transmitted intensities, μ is the linear attenuation coefficient and x is the distance that the photon travels through the medium. In radiology, attenuation can be explained as intensity and dose where the medium is the tissue. Intensity attenuation refers to the reduction in the intensity of the beam as it passes through the tissue, while dose attenuation refers to the reduction in the amount of radiation absorbed by tissue as it passes through it. In this study we emphasized the intensity attenuation by anti-scatter grid as a reference to ESD measurements.

The effects of radiation on living cells could be summarized through two primary mechanisms: direct and indirect adverse effects [9][10][11][12]. Direct effects occur when radiation ionizes DNA atoms, potentially causing considerable damage. If extensive, this damage can prevent proper chromosome replication or alter DNA information, leading to cell death due to direct ionization [13]. Since living cells are primarily composed of water, radiation interacts with it, leading to indirect effects by producing radicals such as H, OH, and in final toxic H_2O_2 [14][15][16]. Given these risks, current research is focused on designing novel devices that reduce radiation dose while maintaining sufficient image quality for diagnostic purposes.

Like all other imaging concepts, digital detectors have replaced conventional films in medical imaging. Initially, computed radiography (CR) [17] using the photostimulable storage method was introduced, followed by the widespread adoption of flat panel detectors (FPD) in X-ray diagnostic [18][19][20]. There are two primary types of FPD based on their construction specifications: direct and indirect. In a direct detector there is an outer amorphous selenium (a-Se) layer with a dipole structure. The incident X-ray photon directly converted into an electric charge by forming an electron-vacancy ion pair in the a-Se layer and creates a current. This current is proportional to the photon's energy; detected and converted into an image by thin film transistor (TFT) array [21]. Indirect-type FPD detectors have a scintillator layer of Cesium Iodide (CsI) or Gadolinium Oxysulfide (Gd_2O_2S) on top. This converts X-rays into light photons. Beneath this layer, there are the Amorphous Silicon (a-Si) photodiodes on a TFT array [22][23]. A flat panel detector (FPD) has a two-dimensional photosensitive area. The collimated X-ray beam is directed towards the object in a cone-shaped geometry. The type of beam geometry being referred to is known as a cone beam. Anti-scatter grid placed in front of the FPD.

The grid is a plate with Pb sections in a membrane structure used to improve image quality. When an incident X-ray arrives at the patient part of them are scattered from bones or tissue as shown in Fig.1A. Anti-scatter grid is designed to prevent those scattered photons from reaching the detector [24][25]. Since incident rays are in the cone shape, the grid is

designed to allow direct photons. That is why grids have source to image distance (SID) [26]. The use of a grid is mandatory, especially when tissue thickness was increased [27][28]. Using an anti-scatter grid can increase the patient's entrance dose because the primary beam may require an increase in intensity to compensate for the absorption of X-rays by the grid. The decision to use an anti-scatter grid thus involves a trade-off between reducing scatter (by enhancing image quality) and minimizing the radiation dose to the patient [29]. That requires careful consideration to balance these factors appropriately. The managing and minimizing of this dose are crucial for patient safety, as excessive radiation can increase the risk of harm and potential long-term effects, such as cancer [30][31].

In LAD system, incident X-ray and the detector's active area are in the same plane and image is performed line by line to form the image Fig.1B. X-ray is fan-shaped and covers photosensitive window of the LAD. In this case, the scattered photons can't reach the detector to distort the image and anti-scatter grid is not required [32].

Due to the possible vibrations caused by scan movement and time elapse, LAD is not yet widely used in in direct radiography. Moreover, scan time should be well arranged considering patient-oriented motion artifact.

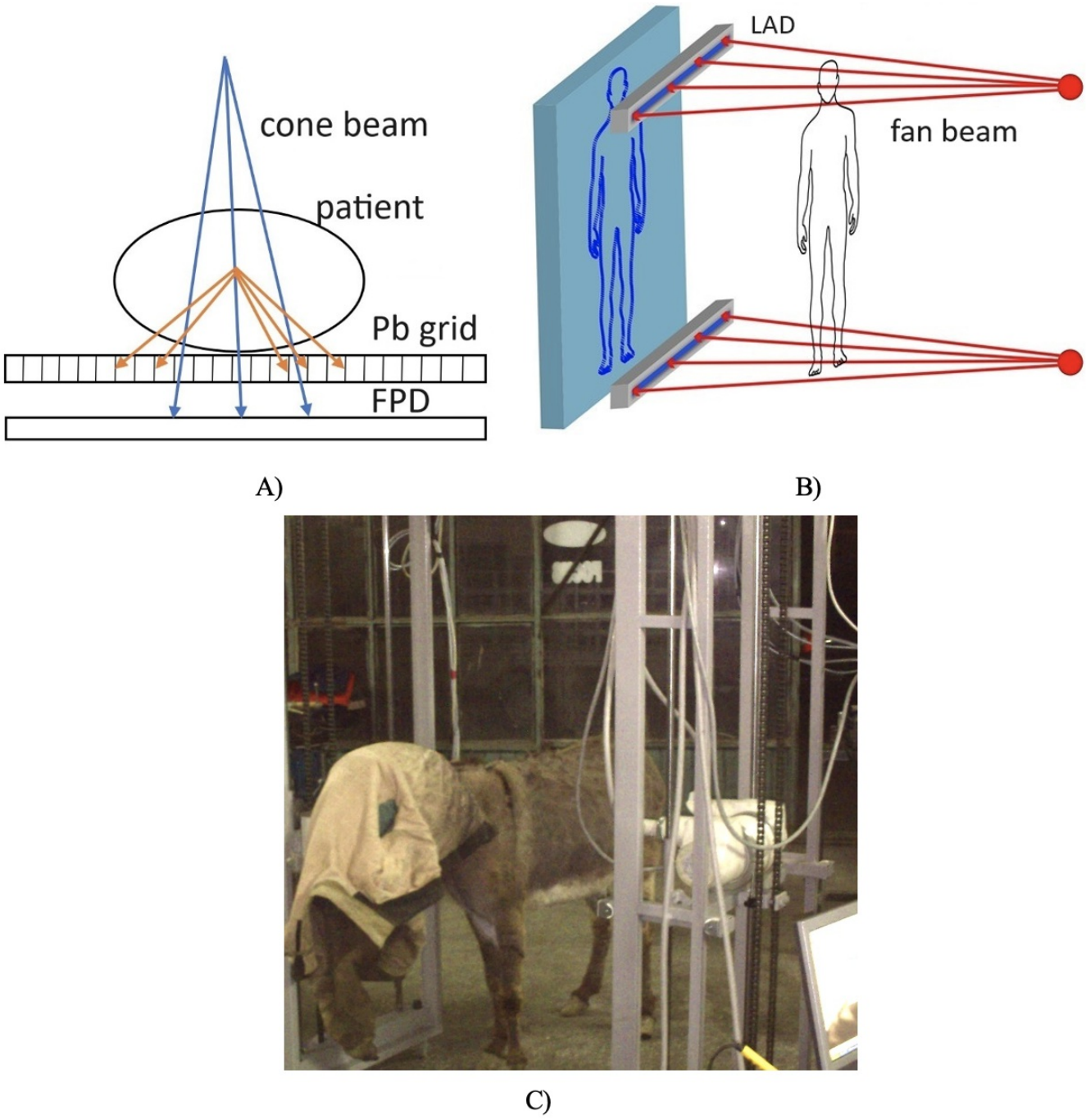

Figure 1. A) FPD and anti-scatter Pb grid which attenuates scattered photons from cone beam and let direct photons to form the image B) LAD with fan beam C) Four years old female donkey.

That is why LAD are widespread in non-destructive testing (NDT) and security areas where LAD and X-ray source are fixed while the object moves on a conveyor [33].

Our prior aim was to perform a study that helps the reduction in ESD in radiography. When we observe the dose reduction that is especially related with the thickness of the tissue in LAD, we evaluated veterinary radiography where thicker tissues should be diagnosed. That is why, we firstly described how medical studies was performed by using anthropomorphic human and water phantom then continued in veterinary diagnostic by imaging four-year-old female

donkey as shown in Fig. 1C.

2. Materials and Methods

To improve the reliability of the study, all the physical and X-ray features of LAD system Fig.1C were designed and manufactured according to the reference FPD system. Both LAD and FPD were chosen as indirect (a-Si) photo diode array type with Gadolinium Oxysulfide scintillator.

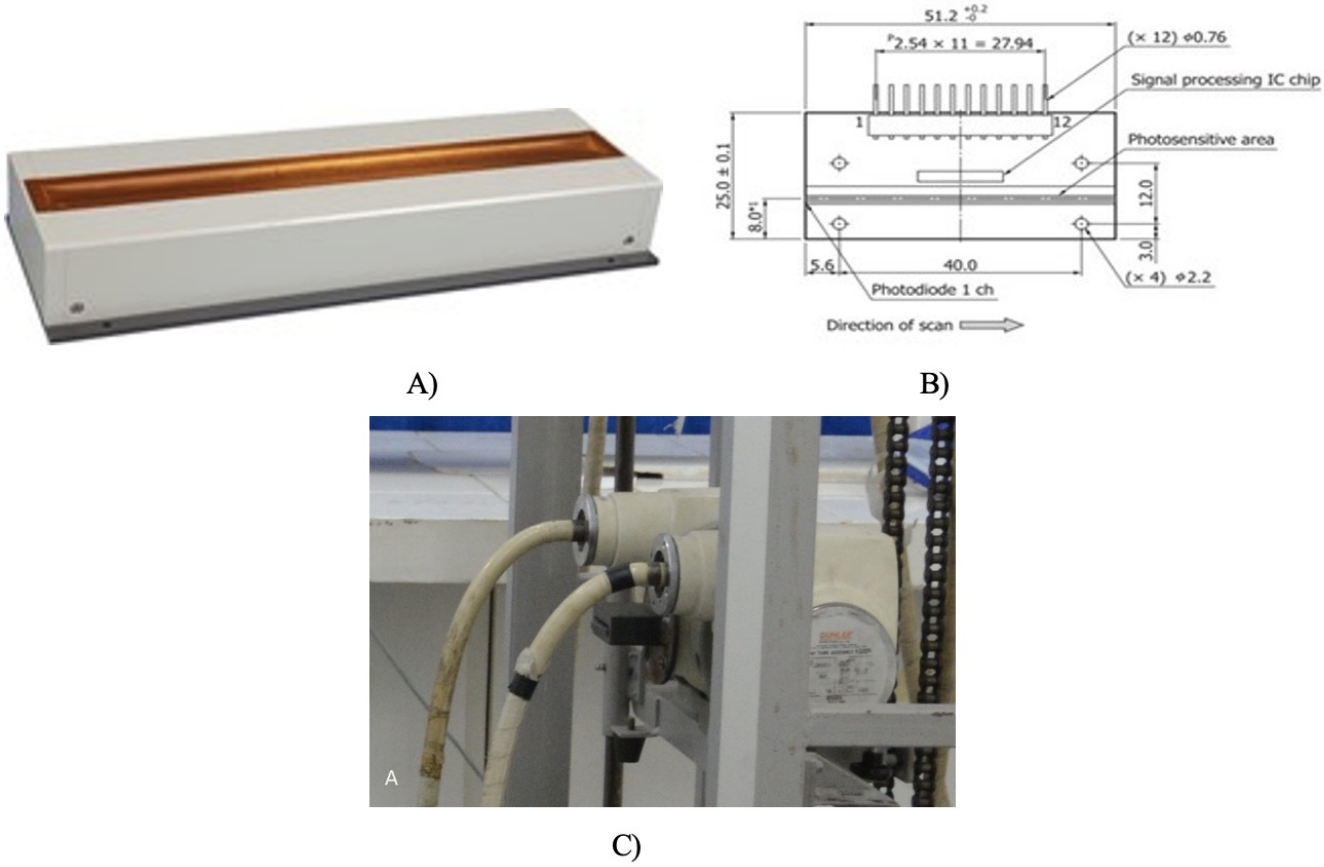

Figure 2. A) Hamamatsu C9750T line scan camera B) One piece of linear array detector in Hamamatsu C9750T C) Pb fan beam collimator attached to the X-ray tube.

X-ray tube and LAD mounted at the same horizontal plane on quadruple bearings so that X-ray scan can be performed at any selected height from 20-210 cm and speed up to 1.2 m/s robotically. Source to image distance (SID) was chosen as 120 cm similar to the FPD reference system.

As LAD Hamamatsu C9750T line scan camera Fig.2A was used[34]. In fact, this detector was built for NDT applications, however the specifications were covering the range of direct radiography examinations from 25 to 160 kVp. In direct radiography, a single image is obtained, whereas in fluoroscopy, a series of images are captured to create a film for diagnostic purposes [35][36]. The key differences stem from the geometry of the introduced X-ray beam, as cone shaped

for FPD and fan shaped for LAD. We emphasize that C9750T captures line by line, resulting in a still radiographic but not fluoroscopic image even though it was named as line scan camera. One piece of linear array detectors in the line scan camera presents in Fig.2B. There are 10 pieces of detectors that make 512 mm width of total detection area in the camera. Whole image of the scanned area was created digitally. The maximum scan time was defined as 1200 ms experimentally. The purpose of faster scans is to avoid motion artifact caused by patient's movements. Imaging at a shorter time is especially important in pediatric imaging [37][38]. Fan beam collimator (Fig.2C) was designed and built from Pb by us so that a fan beam at equal width to LAD's photosensitive area would be projected. Therefore, X-ray source and LAD made simultaneous vertical movement according to selected anatomical site. LAD X-ray unit was composed of Trex TM-80 radiographic fluoroscopic (RF) high voltage (HV) generator (150 kVp – 10.000 mAs), Varian Rad 60 tube with 0.6 mm / 1.2 mm focal spots in Sapphire housing, Varex N4X high voltage cables, Hamamatsu C9750 line scan camera with 200 µm pixel size and 12-bit grayscale spatial resolution.

The reference was DR RAD X3C Nova FA FPD system which has 50KW R generator, Varian Rad 13 tube with 1.0 mm / 2.0 mm focal spots that attached to a ceiling suspension with auto collimator, 17"X17" amorphous silicon detector with 160 µm pixel size and 12-bit grayscale, 96-157 cm SID, 10:1 ratio, fixed anti-scatter grid.

The Best Medical brand TN-RD-90 MOSFET dosimeter was used to measure doses[39][40]. Dosimeter probes were placed on anthropomorphic phantoms and the water phantom for entrance skin dose (ESD) measurements [41]. These X-ray scans using Nova FPD system were performed and the dose measurements were done. In these exams the RSD brand anthropomorphic RS 108 skull and RS 330 upper body phantoms were placed in front of the flat panel detector [42][43][44]. The image quality of X-ray parameters at each anatomical position was assessed by measuring the grayscale of a one cm^2 area at the center of the raw image, as recorded by Digital Imaging and Communications in Medicine (DICOM) software.

Based on these quality standards, the ideal X-ray exposure parameters for each site and position were established. For each position like skull Posterior-Anterior (PA) or lumbar Anterior-Posterior (AP) this reference exposure parameters were kept at the center of deviation and ten more images were taken in diagnostic grayscale range. We increased and decreased the kVp 1-2 steps and recorded AEC mAs. The average doses in mGy and exposure parameters as kVp and mAs were shown in Table.1A.

According that recorded grayscale we made same anthropomorphic phantom analysis by LAD similarly as shown in Fig.3A, 3B, and 3C. Since there was no AEC in LAD, X-ray parameters were chosen manually. Again, ten images were taken for each anatomical position and recorded as seen in Table.1B.

In dose and X-ray parameters we should have made right selections since in LAD the X-ray was in fan beam geometry instead of a cone. MOSFET dosimeter had point size sensor and no calculation was necessary while the active scan area was chosen correctly in its settings. For the kVp and mAs selections we use the central dose reference from FPD raw image's and recorded kVp and mAs when we obtained the same grayscale by LAD. kVp values were written directly however mAs values was obtained by dividing scan time. For example, if 70 kVp and 1000 mAs was selected by Trex TM-80 RF LAD system's operator console and the scan was completed at 200 ms at our servo controlled mechanical system

console. The real mAs of each line of the total image was taken in 1000 / 200 = 5 mAs. It should be noted that in fan beam geometry the X-ray were applied via fan beam collimator as the width of a line and each line was obtained by 5 mAs of the X-ray exposure.

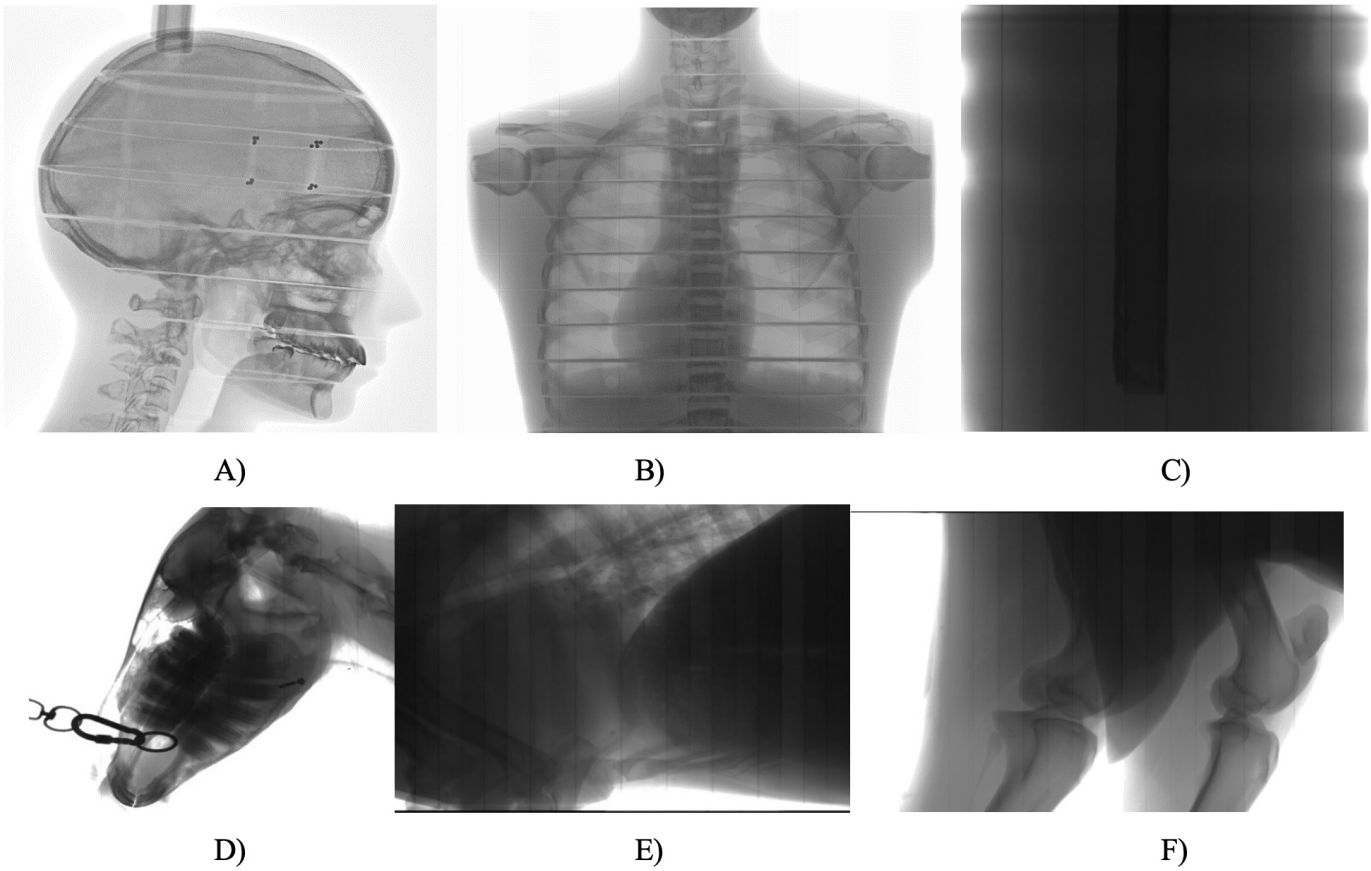

Figure 3. LAD images A) RS108 adult male anthropomorphic phantom skull lateral B) RS 330 adult male anthropomorphic phantom chest PA C) Water phantom at 60 cm water depth while Aluminum bone model was barely recognizable D) Four years old female donkey skull E) Four years old female donkey lumbar F) Four years old female donkey knee.

In this case our analogy was the image obtained at 70 kVp and 5 mAs. Afterwards water phantom was analyzed.

As the water phantom a radiotransparent LEXAN sheet cabinet with a 20 mm layer of Aluminum (Al) block placed inside as a bone model were used to analyze water thickness from 10 to 60 cm. In each depth dependency examination, the depth was incrementally increased by 10 cm. Then we found lowest X-ray parameters that the Al bone model in water was barely visible by DICOM and recorded the doses with respect to the water depth. Afterwards the procedure was repeated by LAD system. These values are shown in Table.1C.

Finally, veterinary imaging using LAD was conducted. Observations indicated that the animal was startled by mechanical movements and sounds. To mitigate this, its eyes and ears were covered with a cloth, and mechanical noises were minimized through lubrication. This approach allowed for the acquisition of diagnostic images (Fig.3D, 3E, and 3F) under the X-ray parameters listed in Table.1D.

3. Results and Discussion

The ESD measured by MOSFET was averaged, and then the standard deviation was calculated for 10 repeated images captured by both the LAD and FPD, concerning the X-ray exposure of anthropomorphic phantoms. The units for the entrance skin dose and standard deviation are defined in milli-gray (mGy). The dose result values were presented in Table.1A and 1B, while the graphical comparison was plotted in Fig.4A based on these values. It was observed that there is a dramatic dose difference between the LAD and FPD in the lumbar AP and lumbar lateral (LAT) examinations. This highlights the requirement for higher kVp and mAs settings for imaging thicker tissues, as compared to the settings used for skull and chest examinations with FPD. For the Skull PA, the ESD was 25.9% lower with the LAD, and for the lumbar LAT, there was a pronounced reduction of 43.6% compared to the FPD. Pb membrane structure of grid was causing higher amount of photon attenuation when the thickness and dose rate according to phantom's anatomical site and position were increased.

Table 1A. FPD doses and X-ray parameters

Anatomical site Anthropomorphic	MOSFET Dosimeter ESD (mGy)	Anatomical Program (kVp)	AEC (mAs)
Skull PA	1.36 ± 0.06	69 - 78	15 - 18
Skull Lateral	1.05 ± 0.07	63 - 65	10 -15
Chest PA	0.31 ± 0.09	78 - 85	7 - 9
Chest Lateral	0.65 ± 0.12	80 - 89	13 - 16
Lumbar AP	3.93 ± 0.04	75 - 83	27 - 34
Lumbar Lateral	6.71 ± 0.02	78 - 92	37 - 48

Table 1B. LAD doses and X-ray parameters

Anatomical site Anthropomorphic	MOSFET Dosimeter ESD (mGy)	Applied kVp	Applied mAs
Skull PA	1.08 ± 0.07	62 - 71	13 - 15
Skull Lateral	0.95 ± 0.08	58 - 63	9 - 12
Chest PA	0.29 ± 0.13	71 - 79	6 - 8
Chest Lateral	0.57 ± 0.11	74 - 81	8 - 11
Lumbar AP	2.87 ± 0.03	64 - 74	20 - 25
Lumbar Lateral	4.67 ± 0.02	68 -77	30 - 38

Table 1C. LAD and FPD water phantom doses according to the water thickness

	10 cm	20 cm	30 cm	40 cm	50 cm	60 cm
LAD ESD (mGy)	0.95	2.98	5.32	14.74	37.48	72.76
FPD ESD (mGy)	1.18	3.85	7.45	31.45	122.34	-

Table 1D. Four years old donkey LAD X-ray parameters

Anatomical site veterinary	Applied kVp	Applied mAs
Skull	64 - 69	13 - 16
Chest	62 - 68	10 - 13
Vertebrae	67 - 76	25 - 33
Lumbar	69 - 78	32 - 44
Femur Oblique	77 - 85	40 - 47

An anthropomorphic phantom is designed to simulate the diagnostic features of X-ray procedure. Obviously anthropomorphic phantom dose analysis couldn't have given precise results since the gray scale and diagnostic quality phenomenon are subjective criteria itself [45]. However, as an idea about our goal, the dose comparison for the anatomical sites was obtained. On the other hand, water phantom is used to determine X-ray doses precisely since water reacts to X-ray photon like tissue by means of absorption and scattering characteristics while it has homogenous structure [46][47]. To further refine our comparison of entrance doses between use of the LAD and FPD, water phantom analysis was performed. Water phantom analysis can be considered alongside anthropomorphic phantom analysis, as it involves measuring the dose from photons that penetrate through homogeneous water and reach the detector in X-ray settings, including the presence of an aluminum block [48].

Image related factors like grayscale or diagnostic quality were not taken into account this water phantom measurements. By 10 cm of water thickness the dose necessary for LAD was 22 % lower than FPD which could be considered in the range of mammography examinations. At a depth of 30 cm, the dose increased by 40%, and at 40 cm, this ratio surged to 113.3%. At 60 cm, neither the aluminum bone model was visible nor was the AEC able to terminate the exposure, resulting in the inability to obtain a dose value with the FPD. Photon attenuation on the grid increased correspondingly with higher doses. Even with the highest X-ray generator settings, an image could not be obtained and AEC could not be terminated the exposure. On the contrary, LAD performed successfully (as shown in Fig.3D). According to the entrance skin dose values from the X-ray settings for our water phantom examination, as mentioned in Table.1C, a graphical comparison for a more detailed analysis between the LAD and FPD is demonstrated in Fig.4B.

The dramatic ESD difference starting from 20cm in Fig.4B can be explained as the following: As water thickness increased by 10 cm steps, the number of scattered then attenuated photons by grid increased respectively [49][50]. That is why, at 50 cm of water depth FPD ESD was 326,4% higher than LAD. At 60 cm, FPD cannot get an image while LAD was obtained as shown in Fig.3C.

It was remarkable that animal's anatomical sites and X-ray parameters for the LAD listed in Table.1D were quite similar to the FPD anthropomorphic phantom parameters in Table.1A. The results obtained using these X-ray parameters indicated that adequate image quality could be achieved with correspondingly lower ESD. The close sizes of donkeys and horses suggest that, in theory, equine whole-body imaging could be successfully performed [51][52]. Considering this advantage and using an X-ray generator capable of delivering high voltages up to 150 kVp and 10,000 mAs, it is also theoretically possible to diagnose cattle.

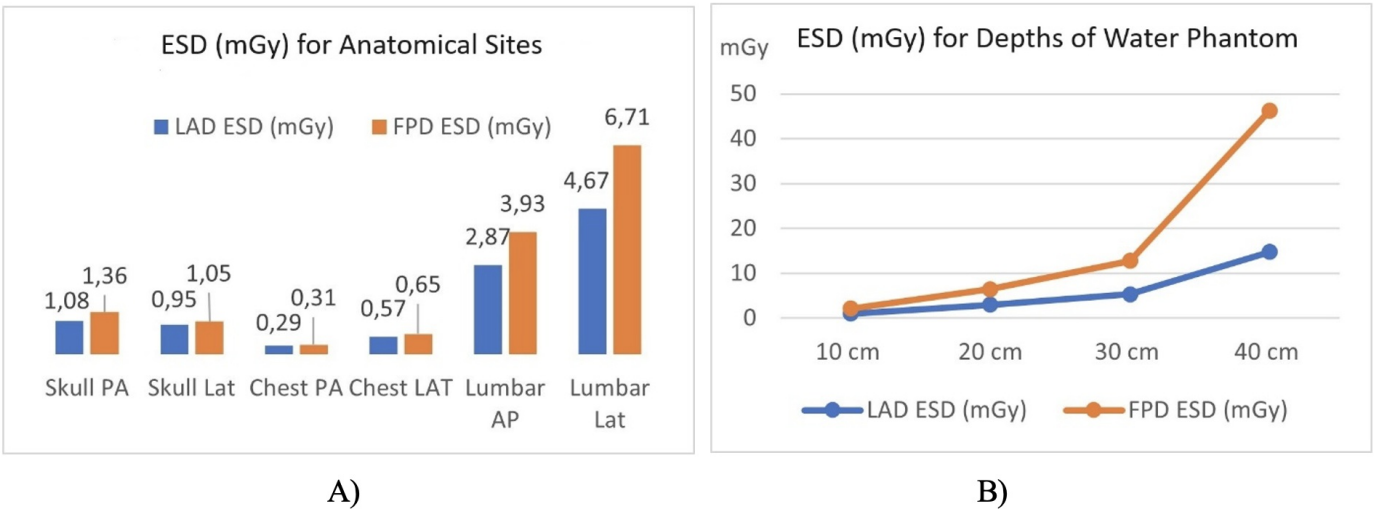

Figure 4. A) Comparison of anthropomorphic phantom entrance skin doses by LAD and FPD. Measured LAD doses are 25.9 % in skull pa and 43.6 % in lumbar lateral lower than FPD. B) Comparison of water phantom doses by LAD and FPD. Measured LAD doses are 22 % at 10 cm, 40% at 30 cm lower than FPD.

LAD system that we designed performs servo-controlled chain driven movement on linear bearings. Although linear double bearings were designed to minimize mechanical vibration, still slight vibration had been observed. During LAD scans vibration was not surprising considering the weight of the vertically moving system. This might be resembled to motion artifacts originated by patient in computed tomography (CT) and despite these vibrations, diagnostic images could be taken [53][54]. In a mechanical design which vibrations are minimized, diagnostic image quality would be increased and ESD might be reduced respectively.

In addition to the dose reduction, magnification with the LAD detector brings a new opportunity. Again, in FPD mammography, magnification is performed even though a grid is used [55]. In FPD patient or object should lean on the grid, otherwise diagnostic quality can't be obtained. However, in our studies with LAD, it has been observed that a higher magnification rate can be achieved by simply moving the object closer to the X-ray source without changing the X-ray parameters. In other words, patient can be located far from the detector and closer to the X-ray source. In this circumstance it is possible to perform higher magnification without loss in image quality. The magnification capability of LAD is a phenomenon may require further researches in direct radiography and mammography.

4. Conclusion

The potential for dose reduction offers benefits not only in human medicine but also in veterinary applications. Currently, X-ray imaging of cattle and equine species is typically difficulties except their extremities. However, our water phantom tests have demonstrated that full-body imaging of large animals is feasible using the LAD system with existing medical X-ray high voltage (HV) generators and tubes. In our study, imaging of a donkey was achieved experimentally using the LAD system, and theoretically, it could be extended to equine and cattle imaging.

Currently, LAD technology is primarily utilized in non-destructive testing (NDT) and security applications, with only a few systems employed in medical radiography. Unlike NDT, where the object is typically stationary while the source and detector move, diagnostic imaging requires the patient to remain still during the imaging process. Our mechanical LAD system was specifically designed and built for experimental dose comparison purposes. During our tests with anthropomorphic phantoms, we achieved diagnostic quality images, although slight mechanical vibrations were observed.

To further refine this technology for direct radiography applications such as mammography or trauma examinations, it is crucial to design and improve the mechanical structures used in LAD systems. By doing so, we could perform diagnostic imaging with significantly lower doses than those currently achieved with FPD systems. Low dose means low energy consumption which may create the chance of producing mobile diagnostic equipment instead of stationary. Additionally, our experience during veterinary scanning highlighted the importance of minimizing noise and reducing scan time. For future systems, replacing chains with belts in the moving components could reduce noise, ensuring that animals remain calm and stationary during imaging. Moreover, a ceiling suspended mechanical system could be more convenient. These adaptations may enhance the practicality and effectiveness of LAD systems in veterinary applications.

Statements and Declarations

Acknowledgements

The authors gratefully acknowledge the partial financial support by Ministry of Industry and Technology B.14.2.KSG.4.07.00.00-150-1392 and Akdeniz University Rectorate Scientific Research Center, (AU-BAP-FYL1787). The experimental procedures were approved by the Local Ethical Committee, Antalya, Turkey and were following the European Union Directive 63/2010.

Competing Interest

The authors declare that no competing interests exist.

References

1. ^*Marcu L, Minh Chau M., Bezak E. How much is too much? Systematic review of cumulative doses from radiological imaging and the risk of cancer in children and young adults. Critical Reviews in Oncology /Hematology, Volume 160, 2021.*
2. ^*Winder M. Owczarek A., Chudek J., Kowalczyk J, Baron J. Are We Overdoing It? Changes in Diagnostic Imaging Workload during the Years 2010–2020 including the Impact of the SARS-CoV-2 Pandemic Healthcare (Basel, Switzerland), 2021.*
3. ^*Charles M. Sources and Effects of Ionizing Radiation. United Nations Scientific Committee on the Effects of Atomic Radiation UNSCEAR 609, 2000.*
4. ^*Keith S., Murray E., Spoo W. Sources of Population Exposure to Ionizing Radiation, Agency for Toxic Substances and Disease Registry ATSDR 243, 1999.*
5. ^*Bosmans H., Marshall N. Radiation doses and Risks Associated with Mammographic screening, Current Radiology Reports Volume 1, 30–38, 2013.*
6. ^*Butler J., Colles C., Dyson S., Kold S., Poulos P., Puchalski S. Grids, Clinical Radiology of the Horse chapter 1, 8, 2017.*
7. ^*Punsmann S., Hellige M., Hoppe J, Freise F, Venner M. Acute interstitial pneumonia in foals: A severe, multifactorial syndrome with lung tissue recovery in surviving foals, Equine Veterinary Journal, 2021.*
8. ^*Votion D., Vandenput S., Duvivier H., Art T., Lekeux P. Analysis of equine scintigraphical lung images, The Veterinary Journal, 1997.*
9. ^*Vaiserman A., Koliada A. Socol Y. Health Impacts of Low-Dose Ionizing Radiation: Current Scientific Debates and Regulatory Issues, Dose Response, 2018.*
10. ^*Nikitaki Z. Mavragani I, Laskaratou D, Gika V., Moskvin V., Theofilatos K. Seminars in Cancer Biology Volumes 37–38, Pages 77-95, 2016.*
11. ^*Weiss G., Mossman K. Ionizing Radiation and Cancer, Radiation Research, Volume 2, Issue 4, 2009.*
12. ^*Alizadeh E., Thomas M. Orlando, Sanche L. Biomolecular Damage Induced by Ionizing Radiation: The Direct and Indirect Effects of Low-Energy Electrons on DNA Annual Review of Physical Chemistry Volume 66, 2015.*
13. ^*Himmetoglu S., Guven F., Bilsel N., Dincer Y. DNA damage in children with scoliosis following X-ray exposure, Minerva Pediatrica 67:1-2, 2015.*
14. ^*Adhikari R. Effect And Application of Ionization Radiation (X-Ray) In Living organism. The Himalayan Physics, 1-2, 89-92, 2012.*
15. ^*Reisz J., BANSAL N., Qian J., Zhao W., Furdui C. Effects of Ionizing Radiation on Biological Molecules-Mechanisms of Damage and Emerging Methods of Detection, Antioxidants & Redox Signaling VOL. 21, NO. 260–292, 2014.*
16. ^*Wang W., Zengliang Y., Wenhui S. Ion irradiation and biomolecular radiation damage II. Indirect effect, Biological Physics, 2010.*
17. ^*Seeram S. Computed Radiography: Physics and Technology, Digital Radiography 41 – 63, 2019.*
18. ^*Cowen A., Kengyelics M., Davies A. Clinical Radiology, Solid-state, flat-panel, digital radiography detectors and their physical imaging characteristics, Clinical Radiology, Volume 63, Issue 5, 487-498, 2008.*
19. ^*Yaffe M., Rowlands J. X-ray detectors for digital radiography, Physics in Medicine & Biology 42, 1–39, 1997.*

20. ^Seibert A. Flat-panel detectors: how much better are they? Pediatric Radiology Volume 36, 173–181, 2006.
21. ^Chen F., Wang K, Fang Y, Allec N. Belev G., Kasap S., Karim K. Direct-Conversion X-Ray Detector Using Lateral Amorphous Selenium Structure IEEE Sensors Journal, Volume: 11 Issue: 2, 2011.
22. ^Floyd C, Warp R., Dobbins J., Chotas H., Baydush H., Voracek R., Ravin C. Imaging Characteristics of an Amorphous Silicon Flat-Panel Detector for Digital Chest Radiography, Radiology V. 218, NO. 3, 2001.
23. ^Paul G., Aufrichtig R. Performance of a 41×41amorphous silicon flat panel x-ray detector for radiographic imaging applications, Medical Physics, 2000.
24. ^Lendl M. Optimized anti-scatter grids for flat panel detectors, Physics of Medical Imaging Volume 6510, 2007.
25. ^Chan H., Lam K., Wu Y. Studies of performance of ant scatter grids in digital radiography: Effect on signal-to-noise ratio, Medical Physics Volume17, Issue4, 655-664, 1990.
26. ^Sabic I. The Effect of Anti-Scatter Grid on Radiation Dose in Chest Radiography in Children, Paediatrics Today 75-80, 2016.
27. ^Martin J. Optimization in general radiography, Biomed Imaging Intervention Journal, 2007.
28. ^Kawashima H., Ichikawa K., Kitao A., Matsubara T., Sugiura T., Kobayashi T., Kobayashi S. Radiation dose considerations in digital radiography with an anti-scatter grid: A study using adult and pediatric phantoms, Medical Physics Volume24, Issue 9, 2023.
29. ^Sigmund P. Part 3. Interatomic Potentials, Scattering and Nuclear Stopping, Particle Penetration and Radiation Effects, Volume 2, 235-276, 2014.
30. ^Linet M., Slovis T., Miller D., Kleinerman R., Lee C., Rajaman P., GONZALEZ A. Cancer risks associated with external radiation from diagnostic imaging procedures CA: A cancer journal of clinicians, Volume 62, Issue 2, 75 – 100, 2012.
31. ^Lin E. Radiation risk from medical imaging, Mayo Clinic Proceedings, Volume 85, Issue 12, 1142- 1146, 2010.
32. ^Sones R., Lauro K., Cattell C. A detector for scanned projection radiography, Radiology Volume 175, No. 2, 1990.
33. ^Wang J., Miao C., Wang W., Lu X. Research of x-ray nondestructive detector for high-speed running conveyor belt with steel wire ropes, Engineering, Physics, 2007.
34. ^Hamamatsu. X-Ray Line Scan Camera C9750 at. No. SFAS0017E13 HPK, 2016.
35. ^Krohmer S. Radiography and fluoroscopy, 1920 to the present. RadioGraphics, Vol.9.No.6, 1989.
36. ^Seibert, A. Projection X-ray imaging, radiography, mammography, fluoroscopy, Health Physics, 116(2), 148–156, 2019.
37. ^Don S. Pediatric digital radiography summary overview: state of confusion, Pediatric Radiology, Volume 41, 567–572, 2011.
38. ^Hintenlang J. Williams L., Hintenlang E. A survey of radiation dose associated with pediatric plain-film chest X-ray examinations, Pediatric Radiology, Volume 32, 771–777, 2002.
39. ^Dance D. Chapter 21 Instrumentation for Dosimetry 21.4 Semiconductor Dosimeters, Diagnostic Radiology Physics A Handbook for Teachers and Students IAEA, 535-537, 2014.
40. ^Huda W., Donnely K. Chapter 11 Radiation Dosimetry, RT X-Ray Physics Review, 251-275, 2014.
41. ^Tanabe R., Araki F. Determination of the surface dose of a water phantom using a semiconductor detector for

diagnostic kilovoltage x-ray beams, Physica Medica, 2021.

42. ^*Bliznakova K., Buliev I., Bliznakov Z. Introduction to anthropomorphic phantoms 2-1, 2-40, 3-18, 2018.*
43. ^*Dewerd, L.A., Kissick, M. The Phantoms of Medical and Health Physics Devices for Research and Development, 1-15,89,91-122, 2014.*
44. ^*Charnley C., England A. An option for optimizing the radiographic technique for horizontal beam lateral (HBL) hip radiography when using digital X-ray equipment, Radiography, Volume 22, Issue 2, May 2016, 137-142, 2016.*
45. ^*Ma K., Hogg P., Tootell A., Manning D., Thomas N., Kane T., Kelly J., McKenzie M., Kitching J. Anthropomorphic chest phantom imaging, The potential for dose creep in computed radiography, Radiography, Volume 19, Issue 3 Pages 207-211, 2013.*
46. ^*Gargett A., Briggs A., Booth J. Water equivalence of a solid phantom material for radiation dosimetry applications, Physics Imaging Radiation Oncology, Volume 14, 43-47, 2020.*
47. ^*Shikhaliev P. Dedicated phantom materials for spectral radiography and CT. Physics in Medicine & Biology, Volume 57 Issue 6, 1575, 2012.*
48. ^*Yadav N., Singh M., Mishra S. Tissue-equivalent materials used to develop phantoms in radiation dosimetry, Materials Today: Proceedings, Volume 47, Part 19, 7170-7173, 2021.*
49. ^*Ubeda C.,Vano E., Gonzalez L., Miranda P., Influence of the antiscatter grid on dose and image quality in pediatric interventional cardiology X-ray systems, CCI, 2012*
50. ^*Söderman M., Hannson B., Axelsson B., Radiation Dose and Image Quality in Neuroangiography: Effects of Increased Tube Voltage, Added X-Ray Filtration and Antiscatter Grid Removal, Interventional Neuroradiology, 1998*
51. ^*Mclean A. Comparing the physiological and biochemical parameters of mules and hinnies to horses and donkeys, academia.edu, 2014.*
52. ^*Dierendonck M., Burden F., 4, Rickards K., Loon J. Monitoring Acute Pain in Donkeys with the Equine Utrecht University Scale for Donkeys Composite Pain Assessment (EQUUS-DONKEY-COMPASS) and the Equine Utrecht University Scale for Donkey Facial Assessment of Pain (EQUUS-DONKEY-FAP) Animals (Basel), 2020.*
53. ^*Murphy A, Hacking C, Iflaq P. Motion Artifact, Radiopaedia.org, 2016.*
54. ^*Sun X., Huang F., Lai G., Yu D., Zhang B., Guo B., Ma Z. Motion Artifacts Detection from Computed Tomography Images, Advanced Data Mining Applications ADMA 347–359, 2021.*
55. ^*Fallenberg, L. Dimitrijevic L., Diekmann F. Impact of Magnification Views on the Characterization of Microcalcifications in Digital Mammography, Röfo, 2014.*